OPEN

Effect of second-order magnetic anisotropy on nonlinearity of conductance in CoFeB/MgO/CoFeB magnetic tunnel junction for magnetic sensor devices

Takahiro Ogasawara[1*], Mikihiko Oogane[1,2,3*], Muftah Al-Mahdawi[2,3], Masakiyo Tsunoda[4,3] & Yasuo Ando[1,2,3]

We studied the effect of second-order magnetic anisotropy on the linear conductance output of magnetic tunnel junctions (MTJs) for magnetic-field-sensor applications. Experimentally, CoFeB/MgO/CoFeB-based MTJs were fabricated, and the nonlinearity, NL was evaluated for different thicknesses, t of the CoFeB free layer from the conductance. As increasing t from 1.5 to 2.0 nm, maximum NL, NL^{max} was found to decrease from 1.86 to 0.17% within the dynamic range, $H_d = 1.0$ kOe. For understanding the origin of such NL behavior, a theoretical model based on the Slonczewski model was constructed, wherein the NL was demonstrated to be dependent on both the normalized second-order magnetic anisotropy field of $H_{k2}/|H_k^{eff}|$ and the normalized dynamic range of $H_d/|H_k^{eff}|$. Here, H_k^{eff}, H_{k2}, are the effective and second-order magnetic anisotropy field of the free layer in MTJ. Remarkably, experimental NL^{max} plotted as a function of $H_{k2}/|H_k^{eff}|$ and $H_d/|H_k^{eff}|$, which were measured from FMR technique coincided with the predictions of our model. Based on these experiment and calculation, we conclude that H_{k2} is the origin of NL and strongly influences its magnitude. This finding gives us a guideline for understanding NL and pioneers a new prospective for linear-output MTJ sensors to control sensing properties by H_{k2}.

Magnetic tunnel junctions (MTJs) using a MgO barrier layer have a large tunnel magnetoresistance (TMR) ratio at room temperature[1–6], and this has made them of interest for a number of spintronic applications such as read heads for hard disk drives and magneto-resistive random access memory. In addition to them, we have used such MTJs for making highly sensitive magnetic-field sensors[7–9] that can detect very weak bio-magnetic fields[10]. Furthermore, recent industrial progress has increased the variety of uses of magnetic sensors. For instance, electric vehicles (EVs) are equipped with current monitoring systems that have Hall sensors. Here, using MTJ sensors instead of Hall sensors would offer certain advantages: smaller size, lower power consumption[11] and higher sensitivity[7–9,12]. Magnetic sensors for automobiles must have specific sensing properties: (1) a dynamic range, H_d, over 1 kOe, (2) high sensitivity, and (3) low nonlinearity (NL). Here, H_d is defined as the range of the magnetic field, H, where the sensing properties are evaluated within $|H| < H_d$; for example, $H_d = 1.0$ kOe means the sensing properties are evaluated within -1.0 kOe $< H < 1.0$ kOe. Regarding (1), since MTJ sensors are composed of two ferromagnetic electrodes with orthogonal easy axes, the maximum H_d is determined by the smaller values of the effective anisotropy field, H_k^{eff}, of the free layer or the switching field, H_{sw}, of the pinned layer. Note that the magnetic field is assumed to be applied along the easy axis of the pinned layer. For this reason, utilization of perpendicular magnetic anisotropy (PMA) is especially useful due to the large H_{sw} of perpendicularly synthetic antiferromagnetic (p-SAF) coupled Co/Pt multilayers[13–17] and L1$_0$-ordered MnGa alloy[18]. These perpendicular

[1]Department of Applied Physics, Tohoku University, Sendai, 980-8579, Japan. [2]Center for Science and Innovation in Spintronics (Core Research Cluster) Organization for Advanced Studies, Tohoku University, Sendai, 980-8577, Japan. [3]Center for Spintronics Research Network, Tohoku University, Sendai, 980-8577, Japan. [4]Department of Electronic Engineering, Tohoku University, Sendai, 980-8579, Japan. *email: takahiro.ogasawara.p3@dc.tohoku.ac.jp; oogane@mlab.apph.tohoku.ac.jp

magnetized pinned layers result in a wide dynamic range up to 5.6 kOe[19–22]. Regarding (2), the sensitivity is expressed by the differential coefficient of the TMR curve, which approximately corresponds to the TMR ratio divided by $2|H_k^{eff}|$. Consequently, a high spin polarization and low $|H_k^{eff}|$ are essential for improving sensitivity. Regarding (3), although NL is still not well understood, it is known that its magnitude as evaluated from the resistance, R, or conductance, G, varies due to its reciprocal relationship. The magnitude of NL evaluated using G is found to be smaller than the magnitude evaluated using R[21,22]. According to the previous study, a conductance model taking account of only first-order magnetic anisotropy suggests that G is expressed by $G = G_0(1-P^2H/H_k^{eff})$[21,22], where G_0 is the conductance at $H = 0$, P is the effective spin polarization and H is the magnetic field. This equation means that G is perfectly proportional to H, resulting in NL to be 0 in theory. Although this model can briefly give an interpretation for the smaller NL in G than R, the finite NL in experiment cannot be explained well. Therefore, for the development of magnetic sensor devices, the origin of NL needs to be understood and its manipulation method should be established.

In this work, we fabricated CoFeB/MgO/CoFeB-based MTJs with p-SAF Co/Pt pinned layers and observed the finite NL which are strongly dependent on CoFeB thickness as well as dynamic range of H_d. In order to analyze the experimental results, we focused on higher order magnetic anisotropy of H_{k2} of the free layer and include its effect in the conductance calculation using the Slonczewski model[23] with simultaneous magnetization rotation. The calculation suggests that the maximum NL, NL^{max}, decreases as the normalized second-order anisotropy, $H_{k2}/|H_k^{eff}|$, and the normalized dynamic range, $H_d/|H_k^{eff}|$, decrease. Based on these experimental and theoretical results, the origin and the controlling method of NL will be discussed.

Experimental Method

All the samples were deposited on Si/SiO$_2$ substrates at room temperature by using dc/rf magnetron sputtering with a base pressure less than 1.0×10^{-6} Pa. The stacking structure of the MTJs were Ta(3)/Ru(10)/Pt(2)/[Co(0.28)/Pt(0.16)]$_9$/Co(0.28)/Ru(0.4)/Co(0.28)/[Pt(0.16)/Co(0.28)]$_5$/Ta(0.2)/Co$_{40}$Fe$_{40}$B$_{20}$(1.0)/MgO(2)/Co$_{20}$Fe$_{60}$B$_{20}$(t)/Ta(5)/Ru(8) (thickness in nm). The thickness of the Co$_{20}$Fe$_{60}$B$_{20}$ free layers, t was varied from 1.5 to 2.0 nm. After patterning the samples into circular junctions with diameters of 100 μm by photolithography and Ar ion milling, the MTJs were post-annealed at 300 °C in a vacuum furnace. TMR curves were measured using the dc-four-probe method. To evaluate H_k^{eff} and H_{k2}, we carried out angle-dependent ferromagnetic resonance (FMR) on samples consisting of Ta(3)/MgO(2)/Co$_{20}$Fe$_{60}$B$_{20}$(t)/Ta(5), which corresponds to the free layer of the MTJs. Microwaves with a frequency of 9.4 GHz (X-band) were applied to the TE$_{011}$ cavity holding the sample, and the resonance spectra were lock-in detected. The magnetization curves were measured with a vibrating sample magnetometer (VSM). All measurements were carried out at room temperature.

Experimental Results

Firstly, let us examine the experimentally measured conductances of the MTJs. As shown in Fig. 1(a) depicting the schematic of our fabricated MTJ, we employed the p-SAF Co/Pt multilayers for the pinned layer of MTJ because our Co/Pt multilayer shows large PMA of c.a. 5 Merg/cm^3 and can be coupled via thin Ru spacer, resulting in the strong antiferromagnetic coupling[17]. Therefore, this magnetization robustness against magnetic field due to the strong coupling is favorable for NL measurements in wide range of H_d[21]. Figure 1(b) shows the TMR and conductance ratio for an MTJ with a 1.50-nm-thick CoFeB free layer under the perpendicular magnetic field. The TMR ratio is defined using a typical expression as shown in Eq. (1), which is normalized by the parallel resistance, R_p. On the other hand, since some of our MTJs lack anti-parallel state due to largely negative H_k^{eff} depending on the thickness (see Fig. 2(a)), the conductance ratio are normalized as in Eq. (2) using minimum conductance of G_{min}. However, it should be noted that the magnitude of TMR and conductance ratio can match each other.

$$\text{TMR ratio} = \frac{R(H) - R_p}{R_p} \times 100 \ (\%) \tag{1}$$

$$\text{Conductance ratio} = \frac{G(H) - G_{min}}{G_{min}} \times 100 \ (\%) \tag{2}$$

The results in the Fig. 1(b) show a large TMR ratio, c.a. 166%, even for post-annealing at 300 °C. This is thought to be due to our optimum structure of MTJs with a flat surface[17]. The TMR and the conductance curve show opposite trends against H, because they are in reciprocal relationship with one another, but the magnitudes of TMR and the conductance ratio accord with each other. Taking the conductance ratio curve of Fig. 1(b), for example, the large dip at c.a. ±4 kOe is due to magnetization reversal of the upper [Co/Pt] layer of the p-SAF pinned layer for the antiferromagnetic coupling which corresponds to H_{sw}. The rotation of the magnetization of the free layer appears within c.a. ±1.8 kOe which corresponds to $|H_k^{eff}|$ of the free layer. Notably, the H dependence of the TMR and conductance curves are different within ±1.8 kOe. Since G (R) is proportional (inversely proportional) to $\cos\theta$ of the free layer from the Slonczewski model[24], where θ is the relative angle of magnetizations, the curves have significantly different shapes where the free layer rotates[21,22]. This contributes to the NL determined from G being smaller than the NL determined from R. Figure 1(c) shows the nonlinearity for 1.5-nm-thick CoFeB determined from the conductance ratio at $H_d = 1.0$ kOe using Eq. (3), where G is the conductance, G_{fit} is the linear fitting to G, and $G_{max(min)}$ is the maximum (minimum) G within the range of H_d.

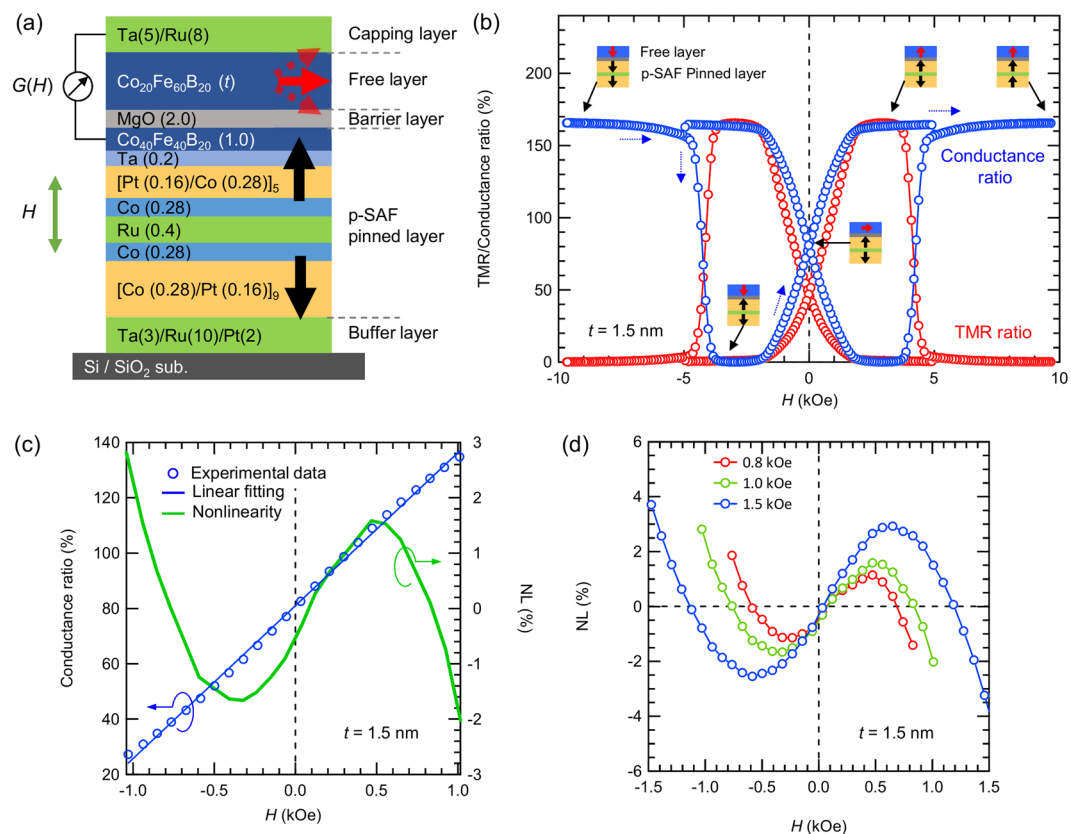$$NL = \frac{G - G_{fit}}{G_{max} - G_{min}} \times 100 \ (\%) \tag{3}$$

Figure 1. (**a**) The schematic of CoFeB/MgO/CoFeB-MTJ using p-SAF coupled [Co/Pt] multilayer via Ru for pinned layer. (**b**) Full scale of TMR and conductance ratio curves as a function of H (red and blue circles, respectively) for 1.5-nm-thick CoFeB free layer. The schematic diagrams show a MTJ consisting of a free layer and p-SAF pinned layers together with the expected magnetization directions for conductance ratio curve under the magnetic field swept from negative to positive. The blue dotted arrows indicate the transition of the conductance ratio curves from negative to positive magnetic field. (**c**) Conductance ratio within the range of ± 1.0 kOe and the NL curve from negative to positive magnetic field. The blue circles and line are experimental and linear fitted data within $H_d = 1.0$ kOe, respectively. The green line is the corresponding NL curve. (**d**) NL curves for different H_d of 0.8, 1.0 and 1.5 kOe for 1.5-nm-thick CoFeB free layer from negative to positive magnetic field.
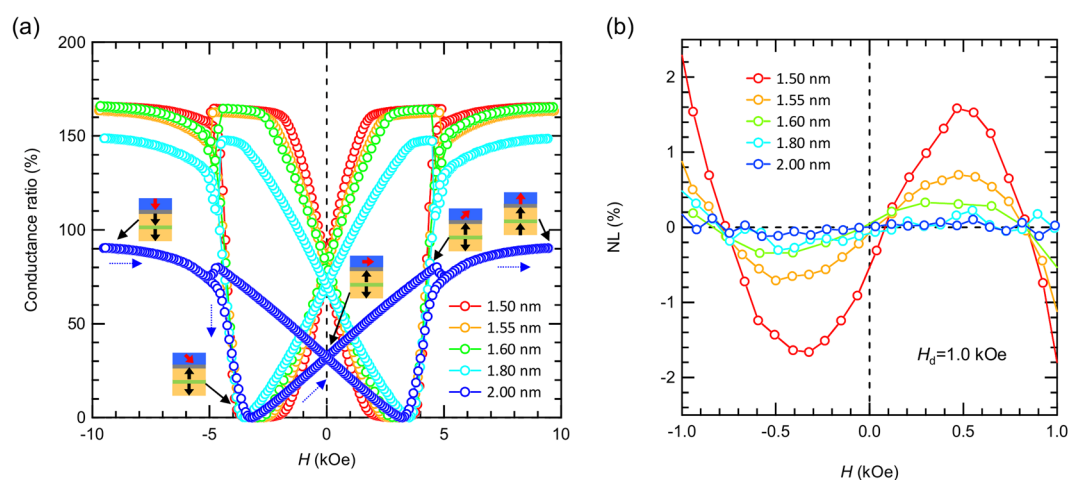

Figure 2. (**a**) Full scale conductance ratio curves for $t = 1.5$–2.0 nm. The schematic diagrams show an expected magnetization in MTJ with 2.0-nm-thick CoFeB under the magnetic field from negative to positive. The blue dotted arrows indicate the transition of the conductance ratio curves from negative to positive magnetic field. (**b**) NL curves for $t = 1.5$ to 2.0 nm from negative to positive magnetic field.
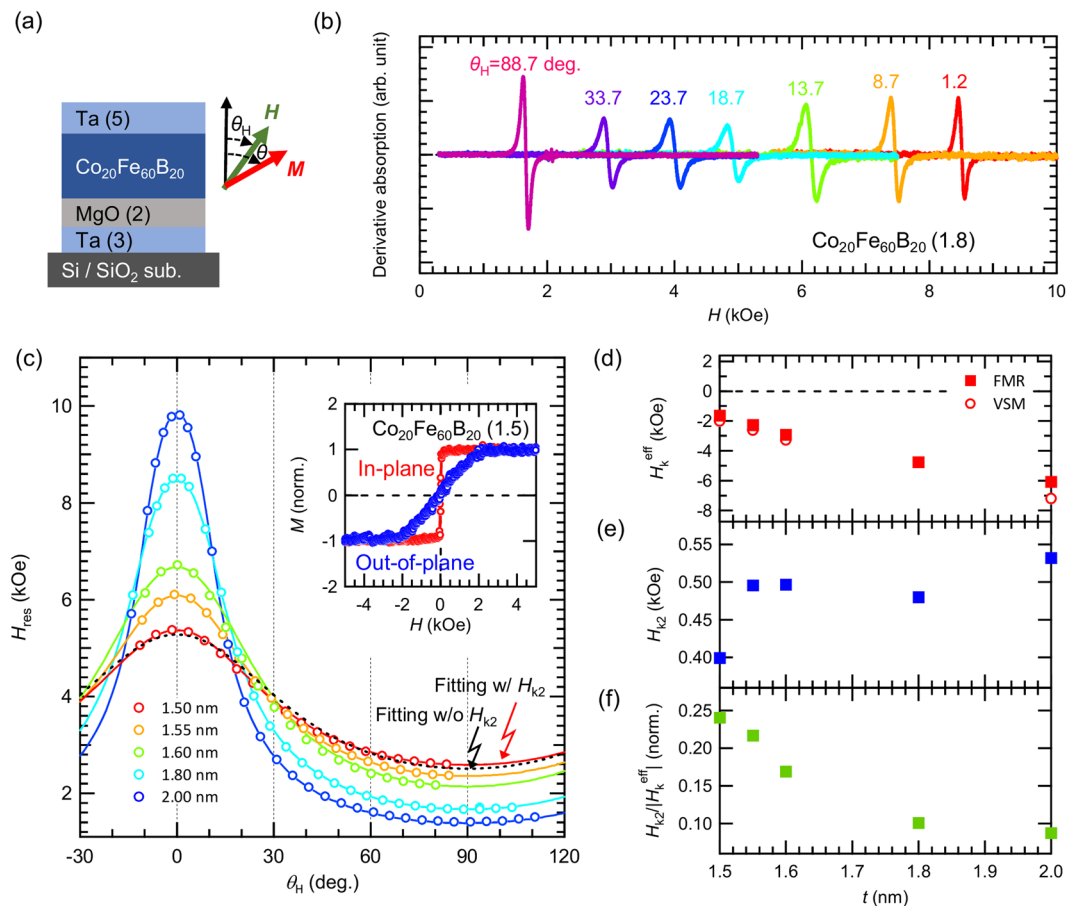
Figure 3. (**a**) Schematic of the sample with MgO/CoFeB/Ta and coordinate system for FMR measurement and analysis. (**b**) Typical FMR spectra for 1.8-nm-thick CoFeB at various magnetic field angle. (**c**) Angular dependent H_{res} data for Ta/MgO/CoFeB (1.5–2.0)/Ta films. Circles and solid lines are experiment and fitting data with H_{k2}, respectively. The black dotted line is the example of the fitting without H_{k2} for 1.5-nm-thick CoFeB. The angles $\theta_H = 0$ and 90 degree correspond to the out-of-plane and in-plane magnetic field from the sample plane. Also, the inset shows the typical magnetization curve of 1.5-nm-thick CoFeB. (**d–f**) Thickness dependence of H_k^{eff}, H_{k2} and $H_{k2}/|H_k^{eff}|$.

This equation quantifies the normalized differences between conductance and its linear fitting and consequently gives H-dependent NL curves. Since NL is expressed by removing a linear component of the fitting from G, the shape of G can be emphasized in H-dependent NL. As shown in Fig. 1(c), slight difference between G and G_{fit} are seen, which gives finite S-shaped NL. Also, we show the H_d dependence of NL for this sample in Fig. 1(d). As increasing H_d from 0.8 to 1.5 kOe, the magnitude of NL increases. Here, the absolute maximum of NL is defined as NL^{max} and it changes from 1.86 to 3.82% in that range. This is due to the increasing of $(G - G_{fit})$ as expanding H_d which means that the difference between experiment and linear fitting is more incorporated by evaluating NL in the larger range of magnetic field.

Figure 2(a) shows the free layer thickness dependence of the conductance ratio of the MTJ with perpendicular magnetic field. For thicker sample, the conductance ratio decreases compared to thinner samples. As increasing t, the H_k^{eff} of free layer negatively increase because the demagnetizing field becomes more dominant than the interfacial magnetic anisotropy. Since the magnetization of the free layer in MTJ starts to rotate at $H \approx H_k^{eff}$ from negative to positive magnetic field, an anti-parallel state cannot be seen in MTJ with negatively large H_k^{eff}. For example, the schematic of Fig. 2(a) shows the expected magnetization of MTJ with 2.0-nm-thick CoFeB free layer. As a 2.0-nm-thick CoFeB exhibits the $H_k^{eff} = -6.2$ kOe (discussed later in Fig. 3(d)), the anti-parallel state becomes absent under the region of the pinned layer showing antiferromagnetic coupling at around $|H| < 4$ kOe. This is the reason for the thickness dependence of the magnitude of the conductance ratio. However, the linear G outputs can be obtained in all samples in the vicinity of $H = 0$. For these samples, NL is evaluated at $H_d = 1.0$ kOe and summarized in Fig. 2(b). This graph shows that NL is highly dependent upon free layer CoFeB thickness. As increasing t from 1.5 to 2.0 nm, NL^{max} decreases from 1.86 to 0.17%. Therefore, it is found that a highly linear G output can be achieved by increasing the thickness, however, this thickness controlling method is not favorable since sensitivity ($\sim$TMR ratio/$2|H_k^{eff}|$) decreases due to negatively larger H_k^{eff} in thick CoFeB. By summarizing our experiments above, NL are strongly dependent on H_d and CoFeB thickness. However, according to the previous conductance model of $G = G_0(1 - P^2 H/H_k^{eff})$ with taking only first magnetic anisotropy[21,22], G is completely linear

to H, where NL is theoretically expected to be zero in all range of H_d and all CoFeB thickness. In order to find clues for understanding the origin and behavior of NL, we characterized the magnetic properties of CoFeB thin films by means of FMR.

Figure 3(a) shows schematic of the sample of MgO/CoFeB/Ta stacks, which corresponds to the free layer of our MTJ and the coordinate system for FMR measurements. For the FMR analysis, the resonance condition based on the Landau-Lifshitz-Gilbert equation can be written as Eqs (4–6), where f is the microwave frequency, γ the gyromagnetic ratio, and H_{res} the resonance field[24,25]. From the angular-dependent H_{res}, the experimental data are fitted by Eqs (4–6) and (8), which in turn give magnetic properties such as H_k^{eff} and H_{k2}.

$$f = \frac{\gamma}{2\pi}\sqrt{H_1 H_2} \tag{4}$$

$$H_1 = H_{res}\cos(\theta - \theta_H) + H_k^{eff}\cos^2\theta - H_{k2}\cos^4\theta \tag{5}$$

$$H_2 = H_{res}\cos(\theta - \theta_H) + H_k^{eff}\cos 2\theta - \frac{1}{2}H_{k2}(\cos 2\theta + \cos 4\theta) \tag{6}$$

For Eq. (7), the magnetic energy density per unit volume for the free layer, E, is well described by summing the Zeeman energy, demagnetizing energy, and magnetic anisotropy. Here, M_s is the saturation magnetization, H and θ_H are the magnetic field and its angle, and K_1 and K_2 are the first- and second-order uniaxial magnetic anisotropy constants, respectively. Also, by the deformation of E as in Eq. (7), we define the coefficient of $\cos^2\theta$ as an effective first-order magnetic anisotropy, K_1^{eff} which is equal to $K_1 + 2K_2 - 2\pi M_s^2$. Since the magnetization angle of the free layer follows $dE/d\theta = 0$, magnetization angle is determined by the first derivative of E described in Eq. (8), where H_k^{eff} is the effective first-order anisotropy field given by $2K_1/M_s + 4K_2/M_s - 4\pi M_s$ and H_{k2} is the second-order anisotropy field given by $4K_2/M_s$.

$$E = -M_s H\cos(\theta_H - \theta) + K_1\sin^2\theta + K_2\sin^4\theta + 2\pi M_s^2\cos^2\theta$$
$$= -M_s H\cos(\theta_H - \theta) - K_1^{eff}\cos^2\theta + K_2\cos^4\theta + K_1 + K_2 \tag{7}$$

$$\sin 2\theta = \frac{2H}{H_k^{eff}}\sin(\theta_H - \theta) + \frac{H_{k2}}{H_k^{eff}}\sin 2\theta\cos^2\theta \tag{8}$$

Figure 3(b) shows typical FMR spectra for 1.8-nm-thick CoFeB at various magnetic field angle. The observed spectra are Lorentzian-like shapes with peak-to-peak line width of several hundred Oe, which is typical for MgO/CoFeB/Ta film due to the spin-pumping effect[25,26]. Figure 3(c) shows the angle-dependent H_{res} for $t = 1.5$–2.0 nm. For all thicknesses, the minimum H_{res} occurs at $\theta_H = 90$ deg., which indicates that all samples exhibit in-plane magnetic anisotropy. The solid lines in Fig. 3(c) are fittings using Eqs (4–6 and (8) with incorporate the effect of H_{k2} to the experimental data and show a good coincidence. It should be noted that if the data is fitted without H_{k2} (i.e. $H_{k2} = 0$), as shown in a black dotted line in Fig. 3(c) for 1.5-nm-thick CoFeB as an example, the differences between the experiment and the fitting becomes larger. Hence, the effect of H_{k2} in our films is not negligible. The best fitting parameter for 1.5-nm-thick CoFeB from FMR is determined as $H_k^{eff} = -1.7$ kOe and $H_{k2} = 0.4$ kOe, which approximately match the results of magnetization curve, displayed in the inset of Fig. 3(c). For the thickness dependence of H_{res}, as t increases, H_{res} at $\theta_H = 0$ deg. increases and that at $\theta_H = 90$ deg. decreases, which suggests that thicker CoFeB film has a negatively larger H_k^{eff} (i.e., larger in-plane magnetic anisotropy). Figure 3(d–f) summarizes the magnetic properties of H_k^{eff} and H_{k2} versus CoFeB thickness as given by the FMR fittings using Eqs (4)-(6) and (8). Also, H_k^{eff} obtained from the magnetization curves from VSM are shown in Fig. 3(d) as the reference. Figure 3(d) shows that H_k^{eff} increases as the CoFeB layer gets thinner, which is due to the presence of a well-defined interfacial magnetic anisotropy[6,27–29]. On the other hand, H_{k2} shows the opposite trend; that is, H_{k2} decreases as t decreases. The reason for this H_{k2} dependence is not clear at present, but there may be effects from the interfacial magnetic anisotropy, even for H_{k2} similarly to H_k^{eff}, since H_{k2} has been reported to depend on the thickness of the CoFeB layer[30]. Some studies have indicated that CoFeB strain and/or surface roughness may increase the magnitude of higher order magnetic anisotropy[31,32]. We consider that the structural and surface properties of CoFeB may vary with the thickness, because CoFeB begins to crystallize from the contacted MgO layer by solid-phase epitaxy and this causes a mixture of bcc and amorphous textures with different interface structures[33]. Therefore, we can infer that, as pointed out above, the effects of the interfacial anisotropy, crystallinity, and interfacial condition are reflected to some extent in H_{k2} of CoFeB films. Figure 3(f) plots $H_{k2}/|H_k^{eff}|$ as a function of t, where FMR fitting results of H_k^{eff} and H_{k2} in Fig. 3(d,e) are used. Remarkably, in our samples, although the ratio of $H_{k2}/|H_k^{eff}|$ is moderate at approximately 0.01 for thicker CoFeB, it increases as decreasing t, resulting in the maximum of $H_{k2}/|H_k^{eff}| = 0.24$ for $t = 1.50$ nm. This result quantitatively suggests that the effect of H_{k2} cannot be negligible for thin CoFeB film. As shown in Eq. (8), since the second-order anisotropy gives additional term of θ dependence for the magnetization rotation, this H_{k2} term is expected to bring some minor change for the conductance curve compared to the model using only first order magnetic anisotropy of $G = G_0(1 - P^2 H/H_k^{eff})$[21,22]. Therefore, second-order magnetic anisotropy possibly is expected to give rise to the finite NL.
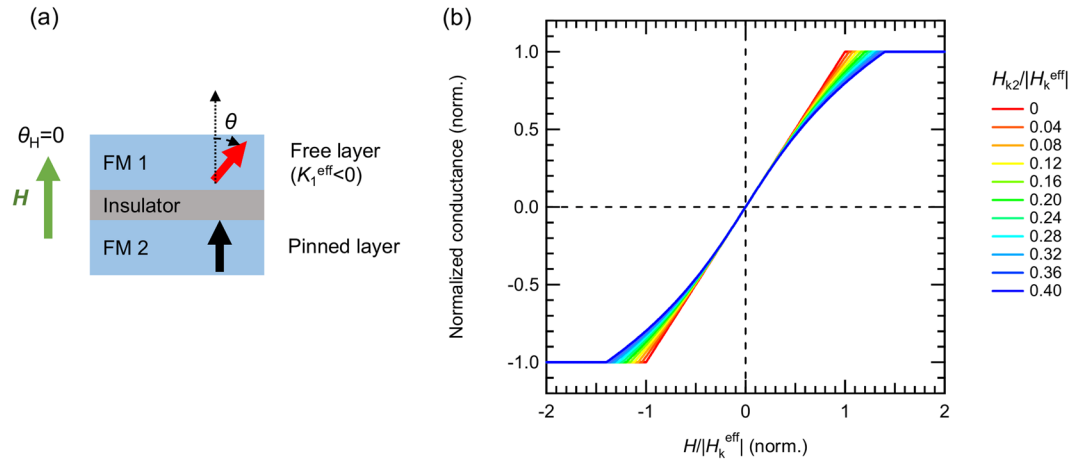
Figure 4. (**a**) Schematic diagram of MTJ consisting of two ferromagnetic layers, FM1 and FM2, with an insulating layer between them. FM1 and FM2 are the in-plane magnetized free layer and perpendicularly magnetized pinned layer, respectively. We assume that the magnetization of FM2 and H is fixed along perpendicular to the film plane. (**b**) Normalized conductance of $(G - G_0)/G_0 P^2$ as a function of $H/|H_k^{eff}|$ for various magnitudes of $H_{k2}/|H_k^{eff}|$.

Model Calculation

Next, let us discuss the effect of second-order magnetic anisotropy on the conductance curves. For the tunnel conductance calculation, we used a Slonczewski model where electrons are transmitted through a rectangular barrier potential. This model can express the TMR phenomena well[23]. The conductance, G, follows Eq. (9), where θ is the angle of the free-layer ferromagnet, measured from the direction normal to the film plane, P is the effective spin polarization and G_0 is the conductance at $\theta = \pi/2$.

$$G = G_0(1 + P^2 \cos\theta) \tag{9}$$

As shown in Fig. 4(a), we assume that the magnetization direction of pinned layer is fixed along the direction perpendicular to the film plane. We also employed a simultaneous rotation model where the magnetization direction rotates following the absolute minimum of the magnetic energy. This means that the first and second derivatives of E of the free layer are in the condition of $dE/d\theta = 0$ (Eq. (8)) and $d^2E/d\theta^2 > 0$. Here, the equation $dE/d\theta = 0$ can be simplified to Eq. (10) under a perpendicular magnetic field with $\theta \neq 0$ or π.

$$\cos\theta = -\frac{H}{H_k^{eff}} + \frac{H_{k2}}{H_k^{eff}}\cos^3\theta \ (\theta_H = 0, \ \theta \neq 0, \ \pi) \tag{10}$$

From Eqs (9) and (10), it is clear that once H_{k2} is 0, G is directly proportional to H. However, a finite value of H_{k2} causes minor changes to the shape of the conductance curves. Here, in Fig. 4(b), we plotted the normalized conductance of $(G - G_0)/G_0 P^2$ against the normalized magnetic field, $H/|H_k^{eff}|$, for different $H_{k2}/|H_k^{eff}|$. The Fig. 4(b) confirms that as $H_{k2}/|H_k^{eff}|$ increases, the conductance curves distinctively change the shapes as expected from Eqs (9) and (10). This is due to the second-order magnetic anisotropy effect.

Figure 5(a) shows the NL curves determined from the conductance curves in Fig. 4(b) by using Eq. (3) for different normalized second-order magnetic anisotropy, $H_{k2}/|H_k^{eff}|$ within the normalized dynamic range $H_d/|H_k^{eff}| = 0.5$. We found that similar S-shaped NL curves observed in our experiment are reproduced in the calculation under $H_{k2} \neq 0$ and it changes to 0 for all range of $H/|H_k^{eff}|$ under $H_{k2} = 0$. Although the shape of NL remains almost unchanged, the magnitude of NL obviously decreases as $H_{k2}/|H_k^{eff}|$ decreases. This calculated result can give an explanation of experimental thickness dependence of NL (see Fig. 2(b)) which is linked to the magnitude of $H_{k2}/|H_k^{eff}|$ (see Fig. 3(f)). Hence, we conclude from these calculations that the observed S-shaped NL curves and the magnitudes originate from the presence of H_{k2}. Additionally, NL can be scaled by the magnitude of $H_d/|H_k^{eff}|$. As shown in Fig. 4(b), G is extremely linear in a very small magnetic field, but not in large magnetic field under $H_{k2}/|H_k^{eff}| \neq 0$. The NL curves with different $H_d/|H_k^{eff}|$ under $H_{k2}/|H_k^{eff}| = 0.2$ are shown in Fig. 5(b). As expected, NL increases with $H_d/|H_k^{eff}|$ due to the curving effect in the large magnetic field from the H_{k2} term. Additionally, this model can briefly explain our results showing an NL^{max} increase in a large dynamic range (see Fig. 1(d)). Figure 5(c) summarizes the calculated NL^{max} against the variation in $H_{k2}/|H_k^{eff}|$ and $H_d/|H_k^{eff}|$. As $|H_k^{eff}|$ increases, both $H_{k2}/|H_k^{eff}|$ and $H_d/|H_k^{eff}|$ decrease, which results in a small NL. However, the reduction in NL by increasing $|H_k^{eff}|$ is in a trade-off relationship with the sensitivity, as mentioned above. In our model that considers second-order magnetic anisotropy, NL decreases with decreasing H_{k2} for all values of $H_d/|H_k^{eff}|$, without the sensitivity deteriorating. Therefore, H_{k2} in the free layer plays an important role and this model gives us a guideline for designing high-performance MTJ sensors.

Consequently, we investigated the correspondence between the experimental and calculated values of NL^{max} for our MTJs with different CoFeB thicknesses of 1.5–2.0 nm which corresponds to the variation of $H_{k2}/|H_k^{eff}|$ of 0.09–0.24 and different H_d of 0.8, 1.0, 1.5 and 2.0 kOe which corresponds to the variation of $H_d/|H_k^{eff}|$ of 0.13–0.89.

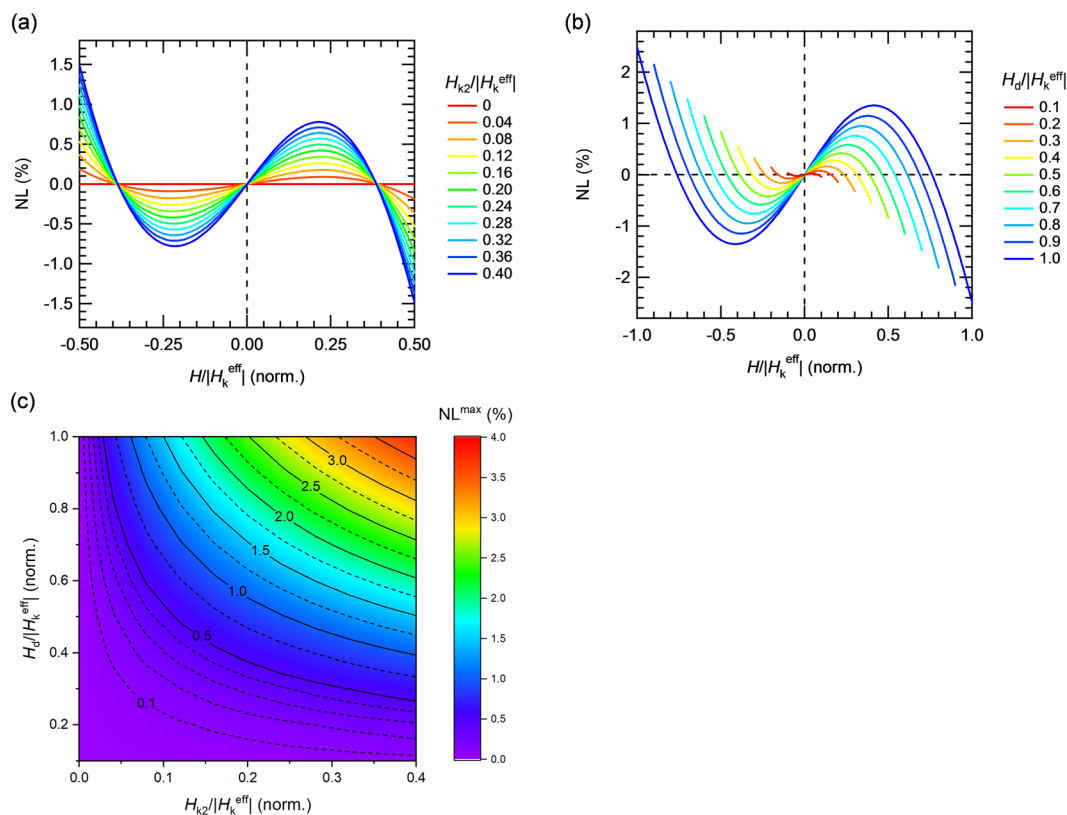**Figure 5.** (**a**) NL curves with $H_d/|H_k^{eff}| = 0.50$ and H_{k2}/H_k^{eff} variations. (**b**) NL curves with $H_{k2}/|H_k^{eff}| = 0.2$ with $H_d/|H_k^{eff}|$ variations. (**c**) Summary of NL^{max} as a function of $H_{k2}/|H_k^{eff}|$ and $H_d/|H_k^{eff}|$.
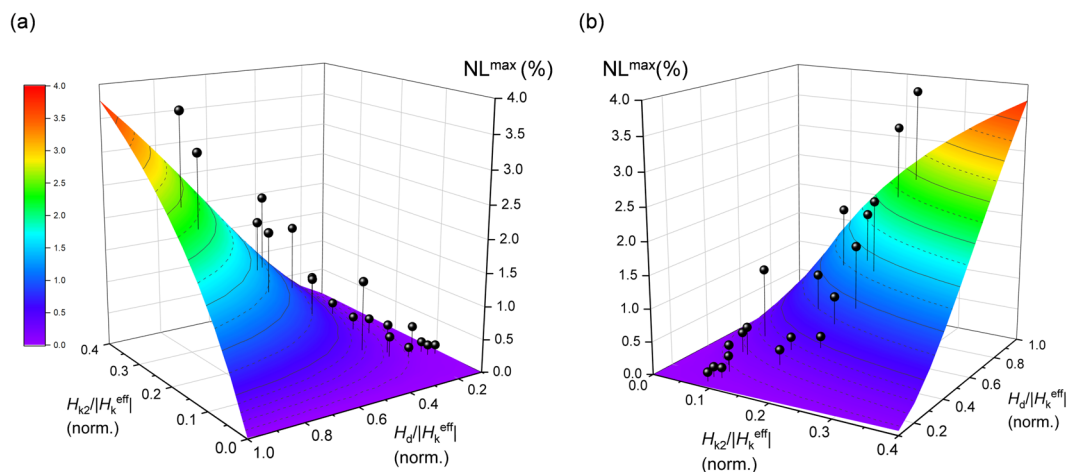

Figure 6. (**a,b**) NL^{max} as a function of $H_{k2}/|H_k^{eff}|$ and $H_d/|H_k^{eff}|$ from different views. The surface and points are calculated and experimental data.

Note that H_d is limited up to 2.0 kOe in order to ensure the magnetic field range with well-fixed pinned layer for NL evaluation. Figure 6(a,b) summarizes NL^{max} as a function of $H_{k2}/|H_k^{eff}|$ and $H_d/|H_k^{eff}|$. The experimental results approximately coincide well with the calculations, that is, as decreasing $H_{k2}/|H_k^{eff}|$ and $H_d/|H_k^{eff}|$, experimental results of NL^{max} decreases. Although a slight discrepancy can be seen resulting in larger NL^{max} which might be due to experimental error or other effects that are not considered in the calculation, such as a slight fluctuations (not a flip but a rotation in microscopic range of the angle) of the pinned layer, angular dispersion, other higher anisotropy terms, and/or tunnel anisotropic magnetoresistance (TAMR) effect, we can approximately explain the NL^{max} trend by $H_{k2}/|H_k^{eff}|$ and $H_d/|H_k^{eff}|$. The details of these minor influence on NL should be the studied more, however, we conclude that predominantly both of $H_{k2}/|H_k^{eff}|$ and $H_d/|H_k^{eff}|$ are intrinsic for NL control.

Conclusion

In conclusion, we studied the effect of second-order magnetic anisotropy on the linearity of the output in MTJ sensors. In experiment, we fabricated CoFeB/MgO/CoFeB-MTJs and S-shaped NL curve are observed in all samples. In addition, for the magnitude of NL, a clear H_d and thickness dependence is found. In order to investigate the origin of NL, we calculated the NL using Slonczewski model with incorporating the effect of second-order magnetic anisotropy. From the calculation, S-shaped NL curve is reproduced under $H_{k2} \neq 0$ and NL^{max} is found to be strongly dependent on both of $H_{k2}/|H_k^{eff}|$ and $H_d/|H_k^{eff}|$. Remarkably, experimental and calculated NL^{max} are in a good agreement, therefore, we conclude that both of $H_{k2}/|H_k^{eff}|$ and $H_d/|H_k^{eff}|$ are intrinsic for NL in MTJ. Thus, this study provides an understanding for the phenomena of NL and pioneers the new method to control sensing properties of MTJ by second-order anisotropy.

References

1. Parkin, S. S. P. *et al*. Giant tunnelling magnetoresistance at room temperature with MgO (100) tunnel barriers. *Nat. Mater.* **3**, 862 (2004).
2. Yuasa, S., Nagahama, T., Fukushima, A., Suzuki, Y. & Ando, K. Giant room-temperature magnetoresistance in single-crystal Fe/MgO/Fe magnetic tunnel junctions. *Nat. Mater.* **3**, 868 (2004).
3. Djayaprawira, D. D. *et al*. 230% room-temperature magnetoresistance in CoFeB/MgO/CoFeB magnetic tunnel junctions. *Appl. Phys. Lett.* **86**, 92502 (2005).
4. Yuasa, S. & Djayaprawira, D. D. Giant tunnel magnetoresistance in magnetic tunnel junctions with a crystalline MgO (001) barrier. *J. Phys. D: Appl. Phys.* **40**, R337–R354 (2007).
5. Ikeda, S. *et al*. Tunnel magnetoresistance of 604% at 300K by suppression of Ta diffusion in CoFeB/MgO/CoFeB pseudo-spin-valves annealed at high temperature. *Appl. Phys. Lett.* **93**, 82508 (2008).
6. Ikeda, S. *et al*. A perpendicular-anisotropy CoFeB-MgO magnetic tunnel junction. *Nat. Mater.* **9**, 721 (2010).
7. Fujiwara, K. *et al*. Fabrication of magnetic tunnel junctions with a bottom synthetic antiferro-coupled free layers for high sensitive magnetic field sensor devices. *J. Appl. Phys.* **111**, 07C710 (2012).
8. Fujiwara, K., Oogane, M., Nishikawa, T., Naganuma, H. & Ando, Y. Detection of Sub-Nano-Tesla Magnetic Field by Integrated Magnetic Tunnel Junctions with Bottom Synthetic Antiferro-Coupled Free Layer. *Jpn. J. Appl. Phys.* **52**, 04CM07 (2013).
9. Kato, D. *et al*. Fabrication of Magnetic Tunnel Junctions with Amorphous CoFeSiB Ferromagnetic Electrode for Magnetic Field Sensor Devices. *Appl. Phys. Express* **6**, 103004 (2013).
10. Fujiwara, K. *et al*. Magnetocardiography and magnetoencephalography measurements at room temperature using tunnel magneto-resistance sensors. *Appl. Phys. Express* **11**, 023001 (2018).
11. Ando, Y. Spintronics technology and device development. *Jpn. J. Appl. Phys.* **54**, 070101 (2015).
12. Jang, Y. *et al*. Magnetic field sensing scheme using CoFeB/MgO/CoFeB tunneling junction with superparamagnetic CoFeB layer. *Appl. Phys. Lett.* **89**, 163119 (2006).
13. Yakushiji, K., Kubota, H., Fukushima, A. & Yuasa, S. Perpendicular magnetic tunnel junctions with strong antiferromagnetic interlayer exchange coupling at first oscillation peak. *Appl. Phys. Express* **8**, 083003 (2015).
14. Chatterjee, J., Tahmasebi, T., Swerts, J., Kar, G. S. & Boeck, J. D. Impact of seed layer on post-annealing behavior of transport and magnetic properties of Co/Pt multilayer-based bottom-pinned perpendicular magnetic tunnel junctions. *Appl. Phys. Express* **8**, 063002 (2015).
15. Lee, J.-B. *et al*. Thermally robust perpendicular Co/Pd-based synthetic antiferromagnetic coupling enabled by a W capping or buffer layer. *Sci. Rep.* **6**, 21324 (2016).
16. Yakushiji, K., Sugihara, A., Fukushima, A., Kubota, H. & Yuasa, S. Very strong antiferromagnetic interlayer exchange coupling with iridium spacer layer for perpendicular magnetic tunnel junctions. *Appl. Phys. Lett.* **110**, 092406 (2017).
17. Ogasawara, T., Oogane, M., Tsunoda, M. & Ando, Y. Large exchange coupling field in perpendicular synthetic antiferromagnetic structures with CoPt alloy. *Jpn. J. Appl. Phys.* **57**, 088004 (2018).
18. Mizukami, S. *et al*. Composition dependence of magnetic properties in perpendicularly magnetized epitaxial thin films of Mn-Ga alloys. *Phys. Rev. B* **85**, 014416 (2012).
19. Nakano, T., Oogane, M., Furuichi, T. & Ando, Y. Magnetic tunnel junctions using perpendicularly magnetized synthetic antiferromagnetic reference layer for wide-dynamic-range magnetic sensors. *Appl. Phys. Lett.* **110**, 012401 (2017).
20. Zhao, X. P. *et al*. L10-MnGa based magnetic tunnel junction for high magnetic field sensor. *J. Phys. D* **50**, 285002 (2017).
21. Nakano, T., Oogane, M., Furuichi, T. & Ando, Y. Magnetic-sensor performance evaluated from magneto-conductance curve in magnetic tunnel junctions using in-plane or perpendicularly magnetized synthetic antiferromagnetic reference layers. *AIP Adv.* **8**, 045011 (2018).
22. Ogasawara, T., Oogane, M., Tsunoda, M. & Ando, Y. Effects of annealing temperature on sensing properties of magnetic-tunnel-junction-based sensors with perpendicular synthetic antiferromagnetic Co/Pt pinned layer. *Jpn. J. Appl. Phys.* **57**, 110308 (2018).
23. Slonczewski, J. C. Conductance and exchange coupling of two ferromagnets separated by a tunneling barrier. *Phys. Rev. B* **39**, 6995 (1989).
24. Beaujour, J.-M., Ravelosona, D., Tudosa, I., Fullerton, E. E. & Kent, A. D. Ferromagnetic resonance linewidth in ultrathin films with perpendicular magnetic anisotropy. *Phys. Rev. B* **80**, 180415 (2009).
25. Iihama, S. *et al*. Damping of Magnetization Precession in Perpendicularly Magnetized CoFeB Alloy Thin Films. *Appl. Phys. Express* **5**, 083001 (2012).
26. Iihama, S. *et al*. Gilbert damping constants of Ta/CoFeB/MgO(Ta) thin films measured by optical detection of precessional magnetization dynamics. *Phys. Rev. B* **89**, 174416 (2014).
27. Wang, W. X. *et al*. The perpendicular anisotropy of $Co_{40}Fe_{40}B_{20}$ sandwiched between Ta and MgO layers and its application in CoFeB/MgO/CoFeB tunnel junction. *Appl. Phys. Lett.* **99**, 012502 (2011).
28. Yang, H. X. *et al*. First-principles investigation of the very large perpendicular magnetic anisotropy at Fe|MgO and Co|MgO interfaces. *Phys. Rev. B* **84**, 054401 (2011).
29. Yakata, S. *et al*. Influence of perpendicular magnetic anisotropy on spin-transfer switching current in CoFeB/MgO/CoFeB magnetic tunnel junctions. *J. Appl. Phys.* **105**, 07D131 (2009).
30. Shaw, J. M. *et al*. Perpendicular Magnetic Anisotropy and Easy Cone State in Ta/$Co_{60}Fe_{20}B_{20}$/MgO. *IEEE Magn. Lett.* **6**, 3500404 (2015).
31. Yu, G. *et al*. Strain-induced modulation of perpendicular magnetic anisotropy in Ta/CoFeB/MgO structures investigated by ferromagnetic resonance. *Appl. Phys. Lett.* **106**, 072402 (2015).
32. Liedke, M. O. *et al*. Magnetic anisotropy engineering: Single-crystalline Fe films on ion eroded ripple surfaces. *Appl. Phys. Lett.* **100**, 242405 (2012).
33. Karthik, S. V. *et al*. Transmission electron microscopy study on the effect of various capping layers on CoFeB/MgO/CoFeB pseudo spin valves annealed at different temperatures. *J. Appl. Phys.* **111**, 083922 (2012).

Acknowledgements

Author contributions

Y.A. and M.O. coordinated the research project. T.O. and M.A. carried out all experiments. T.O. and M.T. performed the theoretical calculation. T.O. wrote the manuscript and all authors discussed the results and reviewed the manuscript.

Competing interests

The authors declare no competing interests.

Additional information

Correspondence and requests for materials should be addressed to T.O. or M.O.

Reprints and permissions information is available at www.nature.com/reprints.

Publisher's note Springer Nature remains neutral with regard to jurisdictional claims in published maps and institutional affiliations.